# Time-Domain Analysis of Periodic Structures at Oblique Incidence: Orthogonal and Nonorthogonal FDTD Implementations

J. Alan Roden, Stephen D. Gedney, *Member, IEEE,* Morris P. Kesler, James G. Maloney, *Member, IEEE,* and Paul H. Harms, *Member, IEEE*

***Abstract*—A novel implementation of periodic boundary conditions incorporated into the finite-difference time-domain (FDTD) technique in both orthogonal and nonorthogonal grids is presented in this paper. The method applied is a field-splitting approach to the discretization of the Floquet-transformed Maxwell equations. As a result, computational burden is reduced and the stability criterion is relaxed. The results of the two methods are compared to experimental data.**

***Index Terms*—FDTD, nonorthogonal, PBG, periodic media.**

## I. Introduction

THE finite-difference time-domain (FDTD) technique is a robust analysis tool applicable to a wide variety of complex problems [1]. It is particularly useful when nonlinearities exist and transient analysis is required. Frequently, problems are encountered in which a periodicity exists in one or more dimension of the problem geometry, as illustrated in Fig. 1(a). Taking advantage of this periodicity can lead to greater efficiency and accuracy when solving the problem numerically.

Typically, each periodic feature is referred to as a cell and the periodicity of these cells is accounted for using Floquet theory. For a normally incident plane wave, accounting for this periodicity in either an orthogonal or nonorthogonal FDTD method is quite straightforward as there is no phase shift between each periodic cell [2]. However, when a plane-wave source is obliquely incident, there is a cell-to-cell phase variation between corresponding points in different unit cells which causes the time-domain implementation to become more difficult.

For oblique incidence plane waves, a Floquet field mapping may be applied, which results in a set of mapped fields which possess the same cell-to-cell field relations as exist for the normally incident unmapped fields [3]. The resulting equations may add considerable complexity to the FDTD solution [4] and lead to a more stringent stability relation for higher angles of incidence. At present, the periodic methods which are available have only been applied using the orthogonal FDTD method.

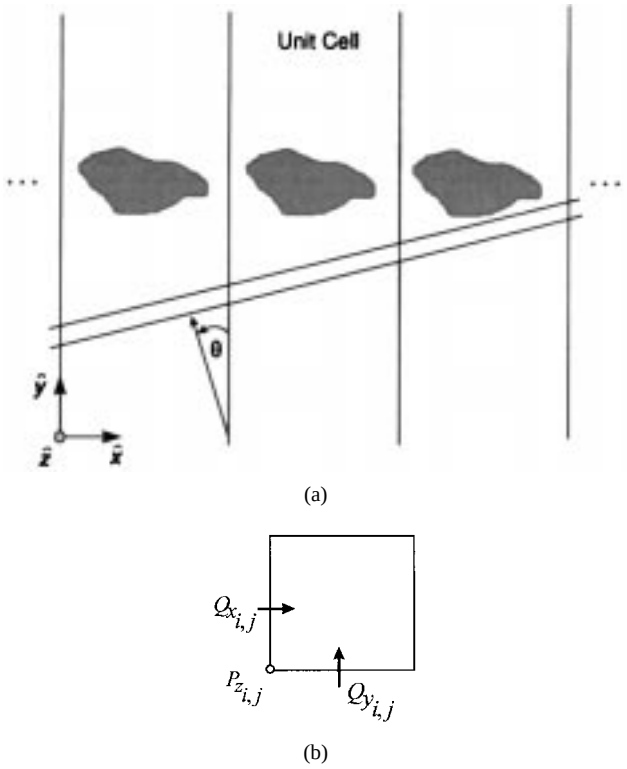


Fig. 1. (a) Periodic geometry in the $\hat{x}$-direction with a plane-wave incident at an angle $\theta$. (b) Typical cell of the computational grid.

In this paper, the Floquet-mapped periodic FDTD equations are solved using an alternative approach referred to as the split-field update method. This technique is shown to be simple to implement and a stability analysis shows the technique to have a less strict stability criterion than previous implementations. The split-field update method is then applied in a general curvilinear space using the nonorthogonal FDTD technique. The use of Floquet-mapped FDTD in nonorthogonal grids may lead to further computational savings due to fewer and

Manuscript received January 14, 1997; revised January 14, 1998. This work was supported in part by the National Science Foundation through the NSF CAREER Award ECS-9624628 and the Army Research Office under Contract DAAHO4-94-G-0243 with the University of Kentucky.

J. A. Roden, M. P. Kesler, J. G. Maloney, and P. H. Harms are with Signature Technologies Laboratory, Georgia Tech. Research Institute, Atlanta, GA 30332 USA.

S. D. Gedney is with the Department of Electrical Engineering, University of Kentucky, Lexington, KY 40506-0046 USA.

Publisher Item Identifier S 0018-9480(98)02753-7.

larger cells. The split-field update technique is validated by comparison of the numerical results with measured data.

## II. Formulation

The field components of a $\mathrm{TM}_z$ plane wave incident on a two-dimensional material which is periodic in the $\hat{x}$-direction [see Fig. 1(a)] will have a phase shift of the form $e^{+jk_x x}$ where $k_x = \frac{\omega \sin\theta}{v_0}$, $v_0$ is the speed of light in free space, and $\theta$ is the angle of propagation for the incident field. A set of auxiliary variables is introduced which implicitly accounts for this phase shift as [3]

$$\begin{aligned} P_z &= \frac{E_z e^{-jk_x x}}{\eta_0} \\ Q_x &= H_x e^{-jk_x x} \\ Q_y &= H_y e^{-jk_x x} \end{aligned} \tag{1}$$

where $\eta_0$ is the impedance of free space.

Substituting these expressions into Maxwell's curl equations maps the solution space such that there is no phase shift between the computed fields at like positions in each periodic cell. Boundary conditions at the periodic boundaries now consist of constraining the tangential fields on opposing boundary walls to be equivalent. The application of this mapping in orthogonal and nonorthogonal grids is now demonstrated.

### A. Orthogonal Grids

Substituting (1) into Maxwell's curl equations leads to

$$j\omega\frac{\epsilon_r P_z}{v_0} = \frac{\partial Q_y}{\partial x} - \frac{\partial Q_x}{\partial y} + \left\{ j\omega\frac{\sin\theta}{v_0} Q_y \right\} \tag{2}$$

$$j\omega\frac{\mu_r Q_x}{v_o} = -\frac{\partial P_z}{\partial y} \tag{3}$$

$$j\omega\frac{\mu_r Q_y}{v_o} = \frac{\partial P_z}{\partial x} + \left\{ j\omega\frac{\sin\theta}{v_0} P_z \right\}. \tag{4}$$

Notice that the substitution of (1) has produced extra terms (denoted by brackets) on the right-hand side of (2) and (4). When (2) and (4) are discretized, the presence of these extra terms leads to difficulty. One difficulty arises due to the appearance of the time derivative ($j\omega \Leftrightarrow \partial/\partial t$) on both sides of these equations. Another difficulty arises because the right-hand sides are no longer spatially aligned. These difficulties may be overcome by introducing dual grids in time and multiple grids in space [4].

In this paper, an alternate approach is taken which is numerically stable, efficient, and applicable in either orthogonal or nonorthogonal grids. The technique used here will be referred to as the split-field update method. Equation (2) is now "split" into two parts by defining $P_z = P_z^a + P_z^b$ where

$$j\omega\frac{\epsilon_r P_z^a}{v_0} = \frac{\partial Q_y}{\partial x} - \frac{\partial Q_x}{\partial y} \tag{5}$$

and

$$P_z^b = \frac{\sin\theta Q_y}{\epsilon_r}. \tag{6}$$

Equation (4) is split similarly by defining $Q_y = Q_y^a + Q_y^b$ where

$$j\omega\frac{\mu_r Q_y^a}{v_o} = \frac{\partial P_z}{\partial x} \tag{7}$$

and

$$Q_y^b = \frac{\sin\theta P_z}{\mu_r}. \tag{8}$$

Substituting the split forms of $P_z$ and $Q_y$ along with (8) into (6) and solving $P_z$ then gives

$$P_z = \frac{P_z^a}{1 - \frac{\sin^2\theta}{\epsilon_r\mu_r}} + \frac{\sin\theta}{\epsilon_r - \frac{\sin^2\theta}{\mu_r}} Q_y^a. \tag{9}$$

Equations (3), (5), and (7)–(9) are discretized using a spatially interleaved Yee lattice [7] (see Fig. 1(b)]. Furthermore, a dual time grid is introduced such that each field component of both $\vec{P}$ and $\vec{Q}$ is computed at each half time step. Note that the time derivatives are applied using central differencing in time as usual, but now these updates are computed at each half time step. Spatial alignment required in (8) and (9) is accomplished by field averaging, which provides second-order accurate results without resorting to multiple spatial grids. The resultant update equations are

$$\begin{aligned} P_{z_{i,j}}^{a^n} = P_{z_{i,j}}^{a^{n-1}} &+ d_{i,j}^x \left( Q_{y_{i,j}}^{n-\frac{1}{2}} - Q_{y_{i-1,j}}^{n-\frac{1}{2}} \right) \\ &- d_{i,j}^y \left( Q_{x_{i,j}}^{n-\frac{1}{2}} - Q_{x_{i,j-1}}^{n-\frac{1}{2}} \right) \end{aligned} \tag{10}$$

$$Q_{x_{i,j}}^n = Q_{x_{i,j}}^{n-1} - b_{i,j}^y \left( P_{z_{i,j+1}}^{n-\frac{1}{2}} - P_{z_{i,j}}^{n-\frac{1}{2}} \right) \tag{11}$$

$$Q_{y_{i,j}}^{a^n} = Q_{y_{i,j}}^{a^{n-1}} + b_{i,j}^x \left( P_{z_{i+1,j}}^{n-\frac{1}{2}} - P_{z_{i,j}}^{n-\frac{1}{2}} \right) \tag{12}$$

$$P_{z_{i,j}}^n = \frac{P_{z_{i,j}}^{a^n} + \frac{\sin\theta}{2\cdot\epsilon_r}(Q_{y_{i,j}}^{a^n} + Q_{y_{i-1,j}}^{a^n})}{1 - \frac{\sin^2\theta}{\mu_r\epsilon_r}} \tag{13}$$

$$Q_{y_{i,j}}^{b^n} = \frac{\sin\theta}{2\mu_r}(P_{z_{i+1,j}}^n + P_{z_{i,j}}^n) \tag{14}$$

where

$$d_{i,j}^x = \frac{v_0\Delta_t}{\epsilon_r\Delta_x} \quad d_{ij}^y = \frac{v_0\Delta_t}{\epsilon_r\Delta_y} \quad b_{i,j}^y = \frac{v_0\Delta_t}{\mu_r\Delta_y} \quad b_{i,j}^x = \frac{v_0\Delta_t}{\mu_r\Delta_x}.$$

Implementation of (10)–(14) showed this technique to be stable for all angles under 90°.

### B. Stability Analysis

In this section, a stability analysis is performed via a Von Neumann technique. Specifically, the fields $Q_x$, $Q_y$, and $P_z$ are initially expanded as a set of plane waves with phase constants $k_x$ and $k_y$. Inserting these field expressions into the combined field updates in (10)–(14) for a fixed $i$, $j$ leads to the second-order difference equation

$$\mathbf{x}^{n+\frac{1}{2}} = -2j[A]\mathbf{x}^n + [I]\mathbf{x}^{n-\frac{1}{2}} \tag{15}$$

where $[I]$ is the identity matrix, $j = \sqrt{-1}$

$$[A] = v_o \Delta_t \begin{bmatrix} 0 & \frac{\sin\theta YC}{\cos^2\theta} & \frac{Y}{\cos^2\theta} \\ 0 & -\frac{\sin\theta XC}{\cos^2\theta} & -\frac{X}{\cos^2\theta} \\ Y & -X\left(1+\frac{C^2\sin^2\theta}{\cos^2\theta}\right) & -\frac{\sin\theta XC}{\cos^2\theta} \end{bmatrix} \quad (16)$$

$$\mathbf{x}^n = \begin{bmatrix} Q^n_{x_{i,j}} \\ Q^a_{y_{i,j}} \\ P^{a^n}_{z_{i,j}} \end{bmatrix} \quad (17)$$

and

$$X = \sin\left(\frac{k_x\Delta_x}{2}\right)/\Delta_x \quad Y = \sin\left(\frac{k_y\Delta_y}{2}\right)/\Delta_y$$
$$C = \cos\left(\frac{k_x\Delta_x}{2}\right) \quad (18)$$

where $C$ arises from the field averaging. This can be reduced to a first-order equation by introducing the vectors [5]

$$\mathbf{y}^{n+\frac{1}{2}} = \begin{bmatrix} \mathbf{x}^{n+\frac{1}{2}} \\ \mathbf{x}^n \end{bmatrix} \quad \mathbf{y}^n = \begin{bmatrix} \mathbf{x}^n \\ \mathbf{x}^{n-\frac{1}{2}} \end{bmatrix} \quad (19)$$

which leads to

$$\mathbf{y}^{n+\frac{1}{2}} = [M]\mathbf{y}^n \quad [M] = \begin{bmatrix} -2j[A] & [I] \\ [I] & 0 \end{bmatrix}. \quad (20)$$

Stability of the first-order equation requires $\rho([M]) < 1$, where $\rho([M])$ is the spectral radius of $[M]$. Due to the characteristics of $[M]$, if $\rho([A]) < 1$, it will follow that $\rho([M]) < 1$. The spectral radius of $[A]$ is governed by its largest eigenvalue. This is found to be (21), shown at the bottom of the page.

Stability requires $|\lambda_{\max}(k_x, k_y)| < 1$ for all $k_x, k_y$. By inspection, the maximum with respect to $k_y$ occurs at $k_y = \frac{\pi}{\Delta_y}$. The most restrictive $k_x$ is not apparent by inspection. By setting the derivative of (21) with respect to $k_x$ equal to zero, it can be shown that the maximum value of (21) occurs when $k_x = \frac{2\xi}{\Delta_x}$ where $\xi$ is defined in (22), shown at the bottom of the page, with $a = (\Delta_x/\Delta_y)^2$. Finally, constraining $|\lambda_{\max}| < 1$ leads to the stability criterion (23), shown at the bottom of the page, where $\xi$ is determined from (22). For $\theta = 0$, (23) reduces to the classical CFL as should be expected.

Equation (23) is an exact stability relation for the algorithm previously described in this section. It is observed that as $\theta$ increases, the stability of the current algorithm is considerably relaxed, as compared to the algorithm presented in [3]. For the square-cell case, Fig. 2 illustrates the ratio, defined as $K_\theta$, of the maximum allowable $\Delta_t$ established by (23) to that of the algorithm in [3] as $\theta$ increases from 0° to 90°. It is observed that nearly a factor of three improvement is realized for larger angles of incidence. This was verified experimentally through FDTD simulations, the results of which are also plotted in Fig. 2. The stability criterion of (23) requires an infinitely small time step at grazing, therefore, other methods may be more practical at extremely large angles.

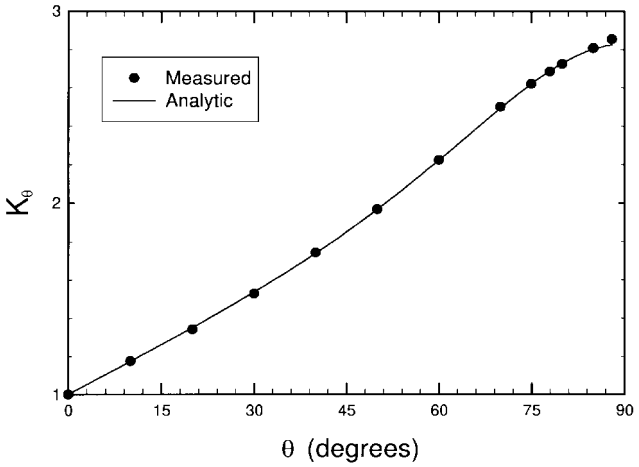


Fig. 2. Stability relation scale factor $K_\theta$ as determined from stability analysis and experimental data.

### C. Nonorthogonal Grids

The split-field update method is now applied in a coordinate system which is nonorthogonal in two dimensions with general curvilinear axes $(u_1, u_2, u_3)$. These axes are defined on a local basis by the unitary vectors $\hat{a}_1$, $\hat{a}_2$, and $\hat{a}_3$ with $\hat{a}_3$ everywhere orthogonal to both $\hat{a}_1$ and $\hat{a}_2$. In the general curvilinear space, the covariant field values are tangential to the unitary vectors and are designated by subscripts. The contravariant field vectors are normal to the cell faces whose edges are defined by the unitary vectors and are designated by superscripts. In the orthogonal space, a solution of the form of (1) was assumed. This solution is now projected onto the general curvilinear axes. The mapping of (1) becomes

$$P_3 = \frac{E_3 e^{-j(\beta_1 u_1 + \beta_2 u_2)}}{\eta_0}$$
$$Q_1 = H_1 e^{-j(\beta_1 u_1 + \beta_2 u_2)}$$
$$Q_2 = H_2 e^{-j(\beta_1 u_1 + \beta_2 u_2)} \quad (24)$$

$$|\lambda_{\max}(k_x, k_y)| = v_o\Delta_t \frac{|\sin\theta|XC + \sqrt{\sin^2\theta X^2C^2 + (X^2+Y^2)\cos^2\theta}}{\cos^2\theta}. \quad (21)$$

$$\xi = \cos^{-1}\left(\frac{1}{2}\sqrt{2\frac{1+\sin^2\theta(4a+2) - \sqrt{\sin^2\theta(a-\sin^2\theta)+1}}{\sin^2\theta(2+3a)+a}}\right) \quad (22)$$

$$\Delta_t < \frac{1}{v_o}\frac{\Delta_x\cos^2\theta}{|\sin\theta|\sin\xi\cos\xi + \sqrt{\sin^2\theta\sin^2\xi\cos^2\xi + (\sin^2\xi + a)\cos^2\theta}} \quad (23)$$

where

$$\beta_1 = k_x \cdot a_{1x} \quad \beta_2 = k_x \cdot a_{2x}.$$

In (24), $a_{1x}$ and $a_{2x}$ represent the $\hat{x}$-directed component of the normalized unitary vectors $\hat{a}_1$ and $\hat{a}_2$, respectively. An equivalent expression to (24) is also used for the contravariant field components.

The mapping of (24) is substituted into the differential form of Maxwell's equations in general curvilinear coordinates [6]. For the $\mathrm{TM}_z$ case, this gives

$$j\omega\frac{\epsilon_r}{v_0}P^3 = \frac{1}{\sqrt{g}}\left(\frac{\partial Q_2}{\partial u_1} - \frac{\partial Q_1}{\partial u_2}\right) + \left\{j\omega\frac{\sin\theta}{v_0\sqrt{g}}a_{1x}Q_2 - j\omega\frac{\sin\theta}{v_0\sqrt{g}}a_{2x}Q_1\right\} \quad (25)$$

$$j\omega\frac{\mu_r}{v_0}Q^1 = -\frac{1}{\sqrt{g}}\frac{\partial P_3}{\partial u_2} - \left\{j\omega\frac{\sin\theta}{v_0\sqrt{g}}a_{2x}P_3\right\} \quad (26)$$

$$j\omega\frac{\mu_r}{v_0}Q^2 = \frac{1}{\sqrt{g}}\frac{\partial P_3}{\partial u_1} + \left\{j\omega\frac{\sin\theta}{v_0\sqrt{g}}a_{1x}P_3\right\}. \quad (27)$$

Notice that the substitution of (24) has produced extra terms (denoted by brackets) on the right-hand side of (25)–(27). Once again, these terms lead to difficulties when these expressions are discretized. The split-field approach is applied in order to discretize these expressions as follows. Equation (25) is split by defining $P^3 = P^{3a} + P^{3b}$ where

$$j\omega\frac{\epsilon_r P^{3a}}{v_0} = \frac{1}{\sqrt{g}}\left(\frac{\partial Q_2}{\partial u_1} - \frac{\partial Q_1}{\partial u_2}\right) \quad (28)$$

$$P^{3b} = \frac{a_{1x}}{\epsilon_r\sqrt{g}}\sin\theta Q_2 - \frac{a_{2x}}{\epsilon_r\sqrt{g}}\sin\theta Q_1. \quad (29)$$

In a like manner, (26) and (27) are split by defining $Q^1 = Q^{1a} + Q^{1b}$, $Q^2 = Q^{2a} + Q^{2b}$ where

$$j\omega\frac{\mu_r Q^{1a}}{v_o} = -\frac{1}{\sqrt{g}}\left(\frac{\partial P_3}{\partial u_2}\right) \quad (30)$$

$$Q^{1b} = -\frac{a_{2x}}{\mu_r\sqrt{g}}\sin\theta P_3 \quad (31)$$

$$j\omega\frac{\mu_r Q^{2a}}{v_o} = \frac{1}{\sqrt{g}}\left(\frac{\partial P_3}{\partial u_1}\right) \quad (32)$$

$$Q^{2b} = \frac{a_{1x}}{\mu_r\sqrt{g}}\sin\theta P_3. \quad (33)$$

Each covariant field component is projected from the contravariant field components by the relation

$$F_i = \sum_{j=1}^{2} g_{ij}F^j \quad (34)$$

with $g_{ij} = \hat{a}_i \cdot \hat{a}_j$ and

$$\sqrt{g} = \hat{a}_3 \cdot (\hat{a}_1 \times \hat{a}_2). \quad (35)$$

In order to solve the auxiliary field expressions of (29), (31) and (33), the split forms of $P_3$, $Q^1$, and $Q^2$ are substituted into (29) giving

$$(P^3 - P^{3a})\epsilon_r = \frac{a_{1x}}{\sqrt{g}}\sin\theta Q_{2a} - \frac{a_{2x}}{\sqrt{g}}\sin\theta Q_{1a} + \frac{a_{1x}}{\sqrt{g}}\sin\theta\left\{\sum_{i=1}^{2} g_{i2}(Q^{ib})\right\} - \frac{a_{2x}}{\sqrt{g}}\sin\theta\left\{\sum_{i=1}^{2} g_{i1}(Q^{ib})\right\}. \quad (36)$$

Equations (31) and (33) are then substituted into (36) and rearranged to give a final expression for $P^3$ as

$$P^3 = \frac{P^{3a} - a_{2x}\frac{\sin\theta}{\epsilon_r\sqrt{g}}Q_{1a} + a_{1x}\frac{\sin\theta}{\epsilon_r\sqrt{g}}Q_{2a}}{1 - \sin\theta\left(\frac{a_{2x}}{\sqrt{g}}M_1 - \frac{a_{1x}}{\sqrt{g}}M_2\right)} \quad (37)$$

where

$$M_1 = \frac{a_{2x}\sin\theta g_{11}}{\epsilon_r\mu_r\sqrt{g}} - \frac{a_{1x}g_{21}\sin\theta}{\epsilon_r\mu_r\sqrt{g}} \quad (38)$$

$$M_2 = \frac{a_{2x}g_{12}\sin\theta}{\epsilon_r\mu_r\sqrt{g}} - \frac{a_{1x}\sin\theta g_{22}}{\epsilon_r\mu_r\sqrt{g}}. \quad (39)$$

## III. Incorporation of the Uniaxial PML Absorbing-Boundary Condition

In this paper, the geometry is periodic in one extent only, the second dimension must be terminated with an absorbing-boundary condition. Periodic structures may require extensive simulation time due to the multiple reflections which occur in setting up the modal distribution on the periodic body. Therefore, an absorbing-boundary condition can cause significant error due to multiple reflections. The perfectly matched layer (PML) absorbing-boundary condition has proven to be far superior to other methods based on differential operators [8]–[10]. The implementation of the uniaxial PML is straightforward [9], [10] and will only be briefly described here. It is assumed that the grid is orthogonal in the outer region of the problem space where the PML resides. Under this assumption, the relevant equations become

$$j\omega\frac{\mu_r Q^{1a}}{v_o}s_2 = -\frac{1}{\sqrt{g}}\left(\frac{\partial P_3}{\partial u_2}\right) \quad (40)$$

$$j\omega\frac{\epsilon_r P^{3a}}{v_0} = \frac{1}{\sqrt{g}}\left(\frac{\partial Q_2}{\partial u_1} - \frac{1}{s_2}\frac{\partial Q_1}{\partial u_2}\right) \quad (41)$$

where

$$s_2 = 1 + \frac{\sigma}{j\omega\epsilon_o}.$$

Equation (40) is a typical FDTD update equation with loss present. Equation (41) is implemented through the introduction of an auxiliary variable. This procedure is described in detail in [10].

## IV. Implementation

FDTD implementation of the nonorthogonal formulation discussed above is presented here. The implementation is very similar to the orthogonal grid case. Equations (28), (30)–(33), and (37) are discretized using a spatially interleaved lattice. Again, a dual time grid is utilized where each field component is computed at each half time step. The resultant update equations are shown in (42)–(47), at the bottom of the page, where $M_1$ and $M_2$ are defined in (38) and (39) and

$$d_{i,j} = \frac{v_0 \Delta_t}{\sqrt{\overline{g}}\epsilon_r} \quad b_{i,j} = \frac{v_0 \Delta_t}{\sqrt{\overline{g}}\mu_r}$$

where

$$\overline{g}_{ij} = \vec{a}_i \cdot \vec{a}_j \quad \sqrt{\overline{g}} = \hat{a}_3 \cdot (\vec{a}_1 \times \vec{a}_2).$$

Note that all field values denoted by underscores are normalized by edge length, while field values denoted by an overscore are weighted by edge length and $l^k_{i,j}$ are reciprocals of edge length.

Spatial averaging is required to spatially align the fields of (45)–(47) as well as the projection operators $\overline{g}_{ij}$ and the vector components $a_{1x}$ and $a_{2x}$. Notice that while the auxiliary variables computed in (46) and (47) must be computed at each half time step, it is not required that they be stored since each update is independent of the past value of the variable. These variables are merely a mathematical convenience.

An exact form for the stability criterion of this method was not derived for nonorthogonal grids. Instead, the stability criterion of irregular nonorthogonal grids [11] was scaled accordingly using the normalized stability criterion derived previously for orthogonal grids giving

$$\Delta_t \lessapprox \frac{K_\theta (1 - \sin\theta)}{v \sup \sqrt{\sum_{i=1}^{2} \overline{g}^{ij}}} \tag{48}$$

where $\overline{g}^{ij} = [\overline{g}_{ij}]^{-1}$ and the sup operator denotes the maximum value throughout all space. This approximation was found to be a conservative guideline for the grids analyzed.

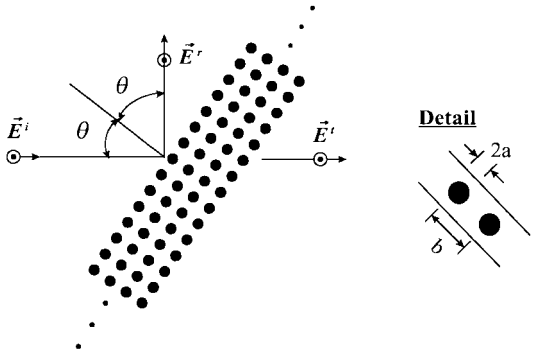


Fig. 3. Cross section of a slab of two-dimensional photonic bandgap material.

## V. Verification

The methods described in this paper were implemented in two numerical analysis codes and verified by studying the scattering properties of a photonic bandgap (PBG) structure. PBG material is the electromagnetic equivalent of the electronic crystal. Many applications exist for these materials including nonmetallic reflectors for antennas [12]. Distinct bandgaps exist in these materials in which no energy will propagate in the crystal at any angle of incidence. This study is not intended to be an exhaustive study of these materials, but simply a verification of the accuracy of this method. The geometry which was studied is illustrated in Fig. 3. Each unit cell consists of four infinitely long dielectric rods with a radius of $a = 2$ mm and a dielectric constant of $\epsilon_r = 4.2$. The rods are arranged in a square lattice such that the center-to-center separation distance $b$ is equal to the unit cell width where $b = 9.0$ mm. A plane-wave source was injected into the Floquet-mapped space using a plane-wave injector of the form $F\left(t - \frac{y \cos\theta}{v_0}\right)$, as explained in [1]. To measure the transmitted field, the mapped fields were integrated in a straight line across a single period in the Floquet-mapped space. Simulations were run at angles of incidence of 0°–50° and experimental data (transmission coefficient) is provided where available.

$$P^{3a^n}_{i,j} = P^{3a^{n-1}}_{i,j} + d_{i,j}\left(\overline{Q}^{n-\frac{1}{2}}_{2i,j} - \overline{Q}^{n-\frac{1}{2}}_{2i-1,j} - \overline{Q}^{n-\frac{1}{2}}_{1i,j} + \overline{Q}^{n-\frac{1}{2}}_{1i,j-1}\right) \tag{42}$$

$$\underline{Q}^{1a^n}_{i,j} = \underline{Q}^{1a^{n-1}}_{i,j} - b_{i,j}\left(P^{n-\frac{1}{2}}_{3i,j+1} - P^{n-\frac{1}{2}}_{3i,j}\right) \tag{43}$$

$$\underline{Q}^{2a^n}_{i,j} = \underline{Q}^{2a^{n-1}}_{i,j} + b_{i,j}\left(P^{n-\frac{1}{2}}_{3i+1,j} - P^{n-\frac{1}{2}}_{3i,j}\right) \tag{44}$$

$$P^{3^n}_{i,j} = \frac{P^{3a^n}_{i,j} - \frac{\sin\theta}{2\cdot\epsilon_r\sqrt{g}}\{a_{2x_i,j}(\overline{Q}^n_{1a_i,j} + \overline{Q}^n_{1a_i,j-1}) - a_{1x_i,j}(\overline{Q}^n_{2a_i,j} + \overline{Q}^n_{2a_{i-1},j})\}}{1 - \sin\theta\left(\frac{a_{2x}}{\sqrt{g}}M_1 - \frac{a_{1x}}{\sqrt{g}}M_2\right)} \tag{45}$$

$$\underline{Q}^{1b^n}_{i,j} = -\frac{l^1_{i,j}\sin\theta}{2\mu_r\sqrt{g}}(a_{2x_i,j+1}P^n_{3i,j+1} + a_{2x_i,j}P^n_{3i,j}) \tag{46}$$

$$\underline{Q}^{2b^n}_{i,j} = \frac{l^2_{i,j}\sin\theta}{2\mu_r\sqrt{g}}(a_{1x_{i+1},j}P^n_{3i+1,j} + a_{1x_i,j}P^n_{3i,j}) \tag{47}$$

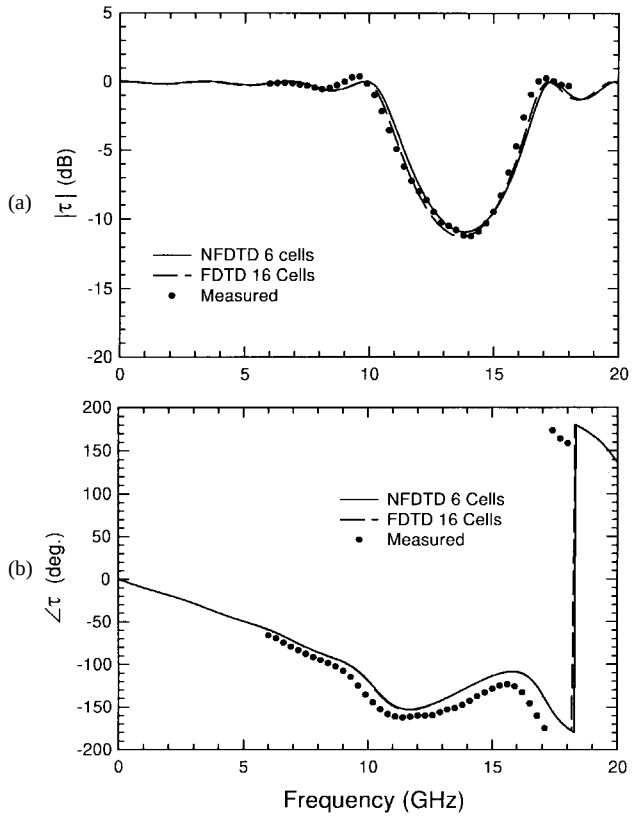


Fig. 4. Transmission coefficient of four rod deep photonic bandgap structure for a plane-wave incident at 0°. (a) Magnitude. (b) Phase. Periodic cell is 9-mm wide and rod diameter is 4 mm, $\varepsilon_r = 4.2$.

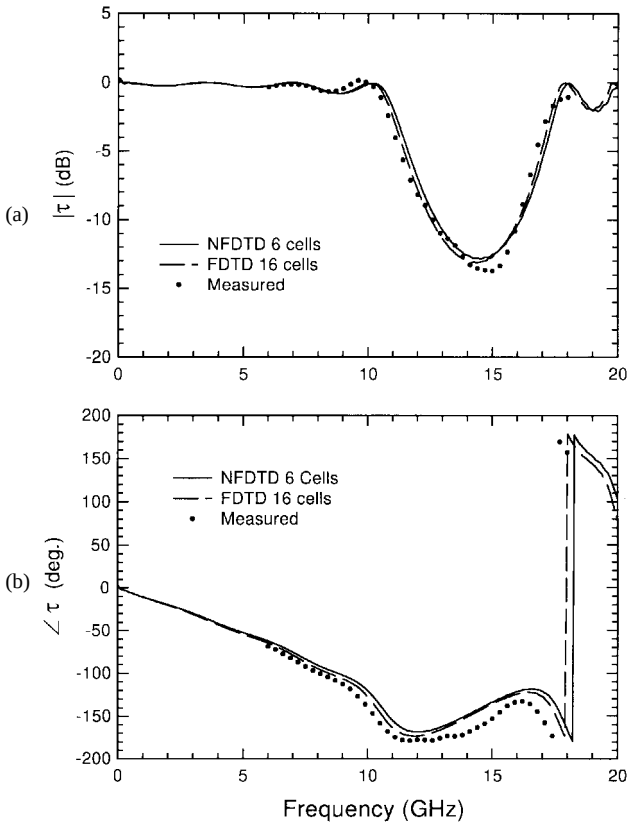


Fig. 5. Transmission coefficient of four rod deep photonic bandgap structure for a plane-wave incident at 20°. (a) Magnitude. (b) Phase. Periodic cell in 9-mm wide and rod diameter is 4 mm, $\varepsilon_r = 4.2$.

This structure was analyzed using both the orthogonal and nonorthogonal implementations formulated in this paper. The orthogonal FDTD code is based on (10)–(14) with each dielectric rod discretized at 16 cells $(\Delta_s = 0.25 \text{ mm})$ across the diameter of rod. The grid dimensions were 38 × 228, including a 10-cell PML region at the two $\hat{y}$-directed walls. Tests were run which showed that the numerical solution had converged at this discretization. In the nonorthogonal FDTD based on (42)–(47), only six cells across the diameter of the dielectric rods were used and the grid dimensions in were 18 × 104 cells, including a ten-cell PML region. For each case, the PML parameters were optimally chosen based on [9]. Measured data was collected using an automated network analyzer and a focus beam measurement system. The dimensions of the periodic model used for measurements were 0.51 m× 0.20 m and the focus beamwidth at the periodic surface was 0.061 m at 8 GHz.

Figs. 4–6 illustrate the level of agreement between the two numerical methods as well as with the measured data. In each case, the level of agreement is quite good and a clear bandgap of at least 10 dB is indicated. The error is very small for either case and probably within the margin of measurable accuracy. When running on a 200-MHz Pentium processor and using a 20° incident field excitation, the nonorthogonal grid code required 1 min to execute while the finely discretized orthogonal grid implementation required 3 min. The orthogonal implementation of this method was stable for all angles of incidence less than 90°. The nonorthogonal method was stable for angles of incidence less than 60°. For angles greater than 60°, the method tended to become unstable in the late time. Similar instabilities are documented for the nonorthogonal FDTD method in an unmapped space in [13].

## VI. Conclusion

A novel implementation of Maxwell equations in a Floquet-transformed space was introduced. This split-field update method was shown to be efficient and simple to implement in both orthogonal and nonorthogonal grids. The stability criterion was derived for orthogonal grids and was more relaxed than previous implementations in the Floquet-transformed space. It was shown that the nonorthogonal FDTD when applied using the split-update method in a Floquet-transformed space resulted in an accurate solution with a much coarser discretization. By comparison of the results from the numerical analysis with measured data, the split-update method was found to be accurate in both orthogonal and nonorthogonal grids. The methods introduced are currently being extended to a three-dimensional space.

## Acknowledgment

The authors express their appreciation to Dr. J. Meadors and the Signature Technologies Laboratory, Georgia Tech. Research Institute (GTRI) for supporting this work. Gratitude

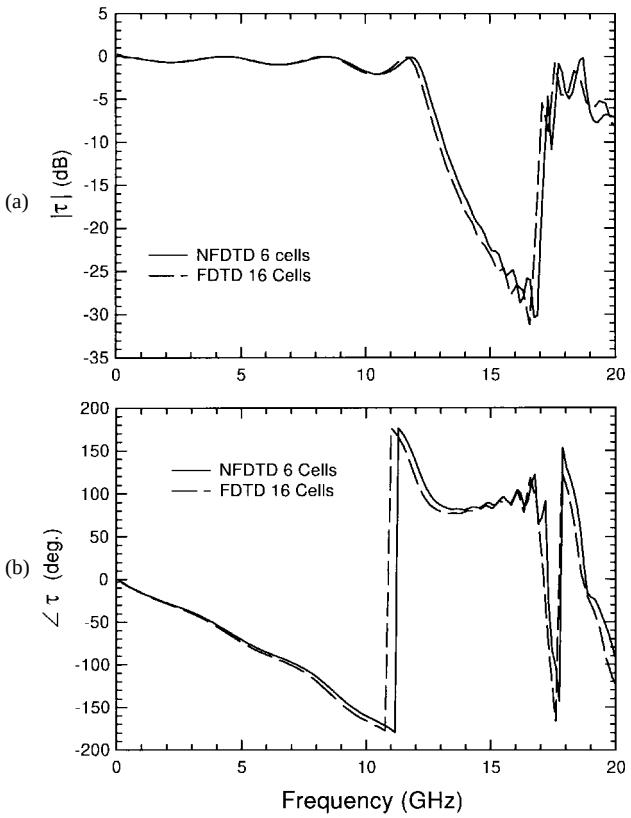


Fig. 6. Transmission coefficient of four rod deep photonic bandgap structure for a plane-wave incident at 50°. (a) Magnitude. (b) Phase. Periodic cell is 9-mm wide and rod diameter is 4 mm, $\varepsilon_r = 4.2$.

also goes to S. Blalock of GTRI for his assistance in providing measured data.

## REFERENCES

[1] A. Taflove, *Computational Electrodynamics: The Finite Difference Time Domain Method.* Norwood, MA: Artech House, 1995.
[2] C. H. Chan, *et al.*, "Electromagnetic scattering of waves by random rough surface: A finite-difference-time-domain-approach," *Microwave Opt. Technol. Lett.*, vol. 4, no. 9, 355–358, 1991.
[3] M. E. Veysoglu, R. T. Shin, and J. A. Kong, "A finite-difference time-domain analysis of wave scattering from periodic surfaces: Oblique incidence case," *J. Electromagnetic Waves Applicat.*, vol. 7, no. 12, 1595–1607, 1993.
[4] Y-C. A. Kao, and R. G. Atkins, "A finite difference-time domain approach for frequency selective surfaces at oblique incidence," in *Proc. IEEE AP-S Int. Symp.*, vol. 2, Baltimore, MD, July 1996, pp. 1432–1435.
[5] S. D. Gedney and U. Navsariwala, "An unconditionally stable implicit finite-element time-domain solution of the vector wave equation," *IEEE Microwave Guided Wave Lett.*, vol. 5, pp. 332–334, Oct. 1995.
[6] J. A. Stratton, *Electromagnetic Theory.* New York: McGraw-Hill, 1941, pp. 38–47.
[7] K. S. Yee, "Numerical solution of initial boundary value problems involving Maxwell's equations in isotropic media," *IEEE Trans. Antennas Propagat.*, vol. AP-14, pp. 302–307, May 1966.
[8] J.-P. Berenger, "A perfectly matched layer for absorption of electromagnetic waves," *J. Comput. Phys.*, vol. 114, no. 1, pp. 185–200, Oct. 1994.
[9] S. D. Gedney, "An anisotropic PML absorbing media for FDTD simulation of fields in lossy dispersive media," *Electromagnetics*, vol. 16, pp. 399–415, July/Aug. 1996.
[10] J. A. Roden and S. D. Gedney, "Efficient implementation of the uniaxial based PML media in three-dimensional nonorthogonal coordinates using the FDTD technique," *Microwave Opt. Technol. Lett.*, vol. 14, no. 2, pp. 71–75, Feb. 1997.
[11] J.-F. Lee, R. Palendah, and R. Mittra, "Modeling three-dimensional discontinuities in waveguides using nonorthogonal FDTD algorithm," *IEEE Trans. Microwave Theory Tech.*, vol. 40, pp. 346–352, Feb. 1992.
[12] M. P. Kesler, J. G. Maloney, B. L. Shirley, and G. S. Smith, "Antenna design with the use of photonic band-gap materials as all-dielectric planar reflectors," *Microwave Opt. Technol. Lett.*, vol. 11, no. 4, pp. 169–174, Mar. 1996.
[13] J. A. Roden "Broadband electromagnetic analysis of complex structures using the finite-difference time-domain technique in general curvilinear coordinates," Ph.D. dissertation, Dept. Elect. Eng., Univ. Kentucky, Lexington, KY, 1997.

**J. Alan Roden** was born on December 29, 1960 in Chattanooga, TN. He received the B.S. degree from the University of Tennessee at Chattanooga in 1984, the M.S. degree in electrical engineering from North Carolina State University at Raleigh, in 1988, and the Ph.D. degree in electrical engineering from the University of Kentucky, Lexington, in 1997.

In 1984, he joined the IBM Corporation, Research Triangle Park, NC, where he was a Product Development Engineer, primarily involved in high-speed communications adapter development. In 1996, he accepted a position with the Georgia Tech. Research Institute, systems. His primary research interest is the application of time-domain numerical methods to large-scale electromagnetic compatibility and radiation problems.

**Stephen D. Gedney** (S'84–M'91) received the B.Eng.-Honors degree from McGill University, Montreal, P.Q., Canada, in 1985, and the M.S. and Ph.D. degrees in electrical engineering from the University of Illinois at Urbana-Champaign, in 1987 and 1991, respectively.

From 1985 to 1987, he worked for the U.S. Army Corps of Engineers, Champaign, IL, where he was engaged in research in EMP pulse simulation and propagation. Since 1991, he has been with the Department of Electrical Engineering, University of Kentucky, Lexington, where he is currently an Associate Professor. From 1992 to 1993, he was a NASA/ASEE Summer Faculty Member at the Jet Propulsion Laboratory, Pasadena, CA, and, in 1996, was a Visiting Professor at Hughes Research Laboratories, Malibu, CA. His current area of research is in the field of computational electromagnetics with emphasis on microwave circuits and antennas, electrical interconnects for VLSI packages, and electromagnetic scattering.

**Morris P. Kesler** received the B.S., M.S., and Ph.D. degrees in electrical engineering from the Massachusetts Institute of Technology, Cambridge, in 1984 and 1988, respectively.

From 1988 to 1990, he was a Post-Doctoral Fellow with IBM Research, Yorktown Heights, NY, and at the IBM Zurich Research Laboratory, where he investigated properties of quantum-well lasers. In 1990, he joined the Georgia Tech. Research Institute, Atlanta, where he is currently a Senior Research Engineer in the Signature Technology Laboratory. His current research interests include electromagnetic materials and scattering, electromagnetic modeling and computation, and adaptive processing techniques.

**James G. Maloney** (S'86–M'92) was born in New York, on August 17, 1965. He received the B.E.E. and Ph.D. degrees from the Georgia Institute of Technology, Atlanta, in 1987 and 1992, respectively.

From 1987 to 1989, he was a Graduate Research and Teaching Assistant at the School of Electrical Engineering, Georgia Institute of Technology, and from 1989 to 1992, he was a J.S.E.P. Fellow. Currently, he is a Senior Research Engineer at the Signature Technology Laboratory, Georgia Tech Research Institute. His current research interests are in application of state-of-the-art computational models, such as FDTD and frequency-domain methods, to the understanding of electromagnetic phenomenology. Specifically, his interest areas include ultrawide-band, transient, conformal, and low-signature antenna and radome systems, advanced electromagnetic materials such as photonic bandgap materials and composite random materials, and acoustical modeling of speech production. He has authored over 25 journal publications and conference papers.

Dr. Maloney was the recipient of the IEEE Antennas and Propagation Society R. W. P. King Best Paper Prize for his paper entitled "Optimization of a conical antenna for pulse radiation: An efficient design using resistive loading" in 1994. Also in 1994, his paper "A study of transient radiation from the Wu-King resistive monopole—FDTD analysis and experimental measurements" was awarded honorable mention for the IEEE Antennas and Propagation Society S. A. Schelkunoff Award.

**Paul H. Harms** (S'80–M'85) received the Ph.D. degree in electrical engineering from the University of Illinois at Urbana-Champaign, in 1992.

He has worked in Post-Doctoral and consulting positions at the University of Illinois and University of Kentucky. He is currently a Research Engineer at the Georgia Tech Research Institute Atlanta. His interests include computational electromagnetics as applied to transmission, radiation, and scattering problems.